A vorticity-divergence view of internal wave generation by tropical cyclones: insights from Super Typhoon Mangkhut

Noel G. Brizuela[1], T. M. Shaun Johnston[1], Matthew H. Alford[1], Olivier Asselin[1], Daniel L. Rudnick[1], James N. Moum[2], Elizabeth J. Thompson[3], Shuguang Wang[4], Chia-Ying Lee[5]

[1]Scripps Institution of Oceanography, University of California, San Diego, La Jolla, CA, USA
[2]College of Earth, Ocean and Atmospheric Science, Oregon State University, Corvallis, OR, USA
[3]NOAA Physical Sciences Laboratory, Boulder, CO, USA
[4]School of Atmospheric Sciences, Nanjing University, Nanjing 210023, China
[5]Lamont-Doherty Earth Observatory, Columbia University, New York, NY, USA

Key Points:

- Internal wave generation by a Super Typhoon explained using float data, linear theory and a 3D model.
- Coupling between ocean vorticity and divergence by Earth's rotation relates wind forcing to thermocline motions and ocean heat transfer.
- Turbulent diffusivities beneath and behind Mangkhut were estimated using Thorpe scales and watermass transformation analyses.

Corresponding author: Noel G. Brizuela, `nogutier@ucsd.edu`

Abstract

Tropical cyclones (TCs) are powered by heat fluxes across the air-sea interface, which are in turn influenced by subsurface physical processes that can modulate storm intensity. Here, we use data from 6 profiling floats to recreate 3D fields of temperature (T), salinity (S), and velocity (u, v, w) around Super Typhoon Mangkhut (western North Pacific, September 2018). Vertical profiles of T and S show the gradual mixing of rainfall and thermocline waters into the mixed layer with diffusivities as high as $\kappa \sim 10^{-1}$ m^2 s^{-1}, causing an asymmetric cold wake of sea surface temperature (SST). A linear model is used to explain observational estimates of vorticity ζ, divergence Γ, and their relation to w. Coupling between ζ and Γ gives rise to near-inertial waves (NIWs) in the TC wake. Observations agree with both output from a 3D coupled model and a linear theoretical statement of inertial pumping. Lastly, we discuss the role of turbulence in rain layer destruction and estimate that $\kappa > 10^{-3}$ m^2 s^{-1} above $\sim$110 m depth up to 600 km behind the TC. These analyses provide an observational summary of the ocean response to TCs, demonstrate the advantages of ζ and Γ for the study of internal wave fields, and provide conceptual clarity on the mechanisms that lead to NIW generation behind TCs.

Plain Language Summary

Near-inertial internal waves (NIWs) are generated by winds and lead to periodic fluctuations in the internal structure of ocean currents and stratification. Turbulence induced by the vertical current shear in these waves is key to sustain the upper ocean stratification and circulation. In this study, we use data from 6 autonomous floats deployed ahead of Super Typhoon Mangkhut to reconstruct the ocean's 3D response. Reconstructed velocity fields agree with output from a coupled 3D model. Linear equations for vorticity and divergence are used to explain patterns in measured currents and NIW generation, as inertial coupling between wind-driven vorticity and divergence pumps the stratified ocean interior. Measurements of temperature and salinity detail how turbulent stirring mixed rainfall and thermocline waters into the upper ocean. Our analyzes indicate that turbulent mixing rates are greatest within 100 km of the typhoon eye but remain elevated hundreds of kilometers behind Mangkhut. Theory and observations presented here provide a comprehensive view of the ocean response to fast-moving, high-intensity tropical cyclones.

1 Introduction

Wind-powered currents that rotate near the inertial frequency (f) dominate upper ocean dynamics behind most tropical cyclones (TCs). On the right (left) side of Northern (Southern) hemisphere storms, transient winds amplify the magnitude of inertial currents, but suppress them on the opposite side (Chang & Anthes, 1978; Price, 1981). Horizontal convergence and divergence associated with these currents lead to inertial pumping of the mixed layer (ML) base. This process transfers ML momentum into near-inertial internal waves (NIWs) that later propagate downwards across the ML base and thermocline (Price, 1983; Gill, 1984; D'Asaro et al., 2007; Sanford et al., 2011; Johnston et al., 2021).

Turbulence and advection associated with near-inertial ML oscillations and NIWs help redistribute heat across subsurface reservoirs. This cools the sea surface temperature (SST) during and shortly after TC passage, reducing subsequent fluxes of heat to the atmosphere and helping modulate storm intensity (K. A. Emanuel, 1999; Glenn et al., 2016). Net changes in SST induced by TCs are often dominated by mixing but depend on a combination of factors including storm intensity, translation speed (U_{storm}), and preceding ocean conditions (Chang & Anthes, 1978; Vincent et al., 2012; Balaguru et al., 2012; Rudzin et al., 2019). Therefore, the mechanisms of air-sea coupling under TCs must be assessed on a regional and storm-by-storm basis (S. Chen et al., 2017).

In this article, we use data from six profiling floats (Johnston et al., 2020) to reconstruct the 3D fields of temperature (T), salinity (S), and currents (u, v, w) beneath Super Typhoon Mangkhut (Fig. 1). Our treatment of the data is validated using output from a coupled 3D ocean-atmosphere model of Mangkhut. Under the assumption that the upper ocean response to TC forcing approaches a steady state when viewed in storm-following coordinates (Geisler, 1970), we diagnose the roles of upwelling, advection, and mixing in the redistribution of subsurface heat and rainfall inputs. Float velocity data are used to validate linear theory results showing that upwelling and NIW generation under TCs result from the coupling of ML vorticity ($\zeta \equiv \frac{\partial v}{\partial x} - \frac{\partial u}{\partial y}$) and divergence ($\Gamma \equiv \frac{\partial u}{\partial x} + \frac{\partial v}{\partial y}$) by Earth's rotation.

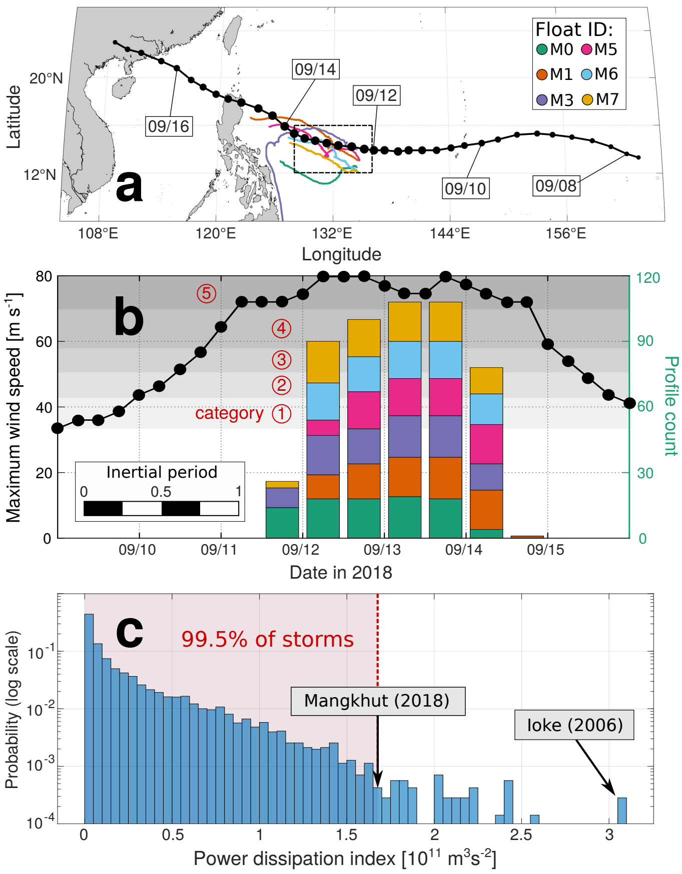

Figure 1. TC overview. (**a**) shows Joint Typhoon Warning Center best track data for Mangkhut. (**b**) shows the maximum 1-minute sustained wind speed $|U_{10}|$ (dotted line, left axis). The histogram in **b** (right axis) shows the time distribution of float measurements used in this study. Gray shading shows the wind speed thresholds for Saffir-Simpson TC categories 1 ($|U_{10}| \leq$ 30 m s $^{-1}$) to 5 ($|U_{10}| > 70$ m s^{-1}). Estimates of power dissipation index for >7000 storms place Mangkhut among the 0.5% most powerful tropical storms in record (**c**).

Section 2 describes our data and processing methods including details about the 3D model used for validation. Section 3 lays out the linear theory of upwelling and NIW generation under TCs and reformulates standard ML dynamics in terms of ζ and Γ to demonstrate their inertial coupling. Section 4 presents observational and modelled maps of (u, v) to verify relations between wind forcing, vorticity, divergence and NIW generation. Indirect evidence of turbulent mixing under Mangkhut is presented using float measurements of T and S in Section 5. A discussion of our methods and results is presented in Section 6, while conclusions are given in Section 7.

2 Data and Methods

Super Typhoon Mangkhut originated on September 7, 2018 as a tropical depression in the central Pacific Ocean and later intensified as it moved westwards into the Philippine Sea. Between September 11 and 15, it sustained maximum 1-minute wind speeds above 70 m s^{-1}, equivalent to a category 5 hurricane. Throughout this period, SOLO-II floats sampled the ocean response under the TC (Fig. 1b). The combination of Mangkhut's long lifespan and elevated intensity put it among the 0.5% most powerful tropical storms on record (Fig. 1c, K. Emanuel 2005). As it travelled through the Philippine and South China Seas, Mangkhut caused significant damage and loss of life in the Philippines, Guam, Taiwan, Hong Kong, and China (Wamsley, 2018).

Upon deployment, SOLO-II floats (R. Davis et al., 2001) modified their buoyancy to dive to 200 m depth and back to the surface at intervals ranging from 35 to 50 minutes. While doing so, they obtained profiles of T and S, and drifted westward with the North-Equatorial Current at ~ 0.18 m s^{-1} (Fig. 2a, Johnston et al. 2020). Because floats record their coordinates at the beginning and end of every dive cycle, their Global Positioning System data allows to produce two estimates of horizontal velocity (Fig. 2b). $\mathbf{u}_{mean}$ is the depth-mean current over the profiling range and is calculated using the difference between the start and end locations of individual dives. Surface estimates $\mathbf{u}_{surf}$, which are subject to wave motion and windage, are calculated using the drift between consecutive dives, when floats remain at the surface for ~ 5 minutes while they transfer data via satellite.

Output from a coupled ocean-atmosphere model of Mangkhut is compared to dynamical insights derived from float velocity data. The coupled system uses the Weather Research and Forecast (WRF) model V3.8.1 (Skamarock et al., 2008) as its atmospheric component, while the ocean is represented by the Hybrid Coordinate Ocean Model V2.2 (HYCOM; Wallcraft et al. 2009). Horizontal grid spacing in HYCOM was 1/12° for 41 vertical layers (10 in the upper 50 m) and output was saved at 3 hour intervals. S. S. Chen & Curcic (2016) give an assessment of this coupled model's performance under North Atlantic TCs. Further details about the model configuration used for Mangkhut were given by Johnston et al. (2021), who first published output from the simulations used here.

Comparisons of model output against measured $\mathbf{u}_{surf}$ (Fig. 3) are indicative of both the accuracy of the simulation and that of float velocity estimates. Although qualitative agreement between both datasets is good, neither float nor model data in Fig. 3 should be regarded as ground truth for ocean conditions at a time and place. While $\mathbf{u}_{surf}$ may be biased by windage or wave motion, the model's atmospheric component lets Mangkhut evolve dynamically, such that the modelled track and intensity differ slightly from observations (Johnston et al., 2021). As described next, objective mapping of float data onto storm-following coordinates may be more representative than pointwise comparisons in Fig. 3.

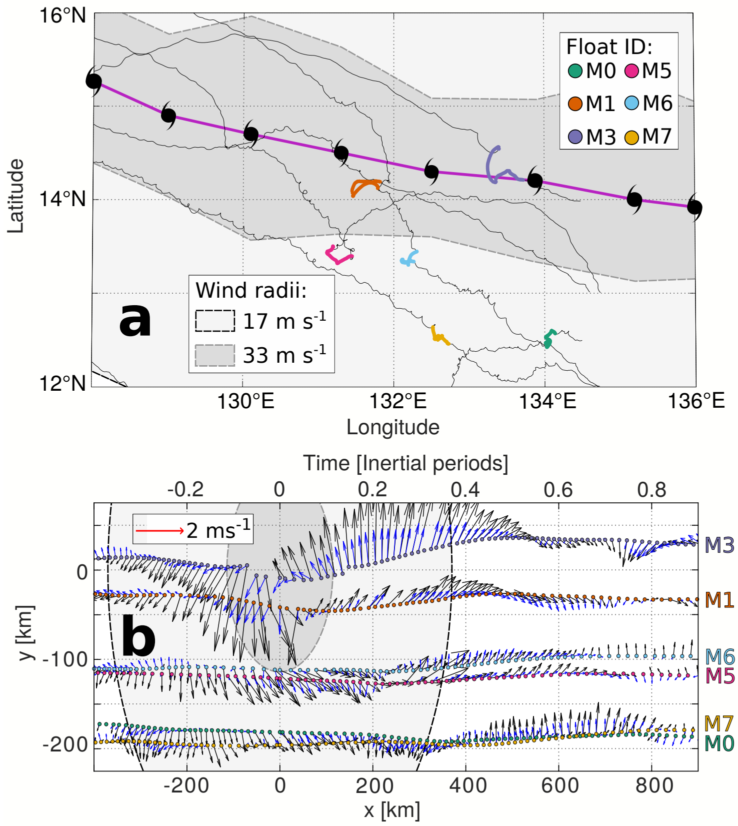

Figure 2. (**a**) shows 6-hourly JTWC best track data for Mangkhut (purple). Black lines mark the trajectories of SOLO-II floats, while the locations of vertical profiles used in this study are highlighted in colors. (**b**) shows $\mathbf{u}_{surf}$ (black) and $\mathbf{u}_{mean}$ (blue) in storm-following coordinates (x, y). Unlike the (x, y) plane, velocity components (u, v) are scaled equally to show the true direction of currents.

2.1 3D reconstruction of the ocean response

Best track data for Mangkhut from the Joint Typhoon Warning Center (JTWC) was linearly interpolated to the times of float data, which were then reorganized in storm-following coordinates (x, y) (Fig. 2b). Positive values of x denote regions behind the storm eye, while $y > 0$ indicates locations right of the TC track. Likewise, $\mathbf{u}_{surf}$ and $\mathbf{u}_{mean}$ were rotated such that u and v represent along-track and cross-track velocities respectively. Plots in (x, y) use the equivalent time $t = x/U_{storm}$ ($U_{storm} = 6.2$ m s^{-1}) to preserve information about temporal variability that has been mapped onto x. Time scaling $t\frac{f}{2\pi}$ uses the inertial period $\frac{2\pi}{f}$ at 15.54°N ($\sim$ 45 hr) such that one inertial period in t corresponds to $U_{storm}\frac{2\pi}{f}$ =1000 km in x (Fig. 2b).

Despite the fact that each float effectively sampled different parts of the storm at different times (Fig. 2a), both $\mathbf{u}_{surf}$ and $\mathbf{u}_{mean}$ line up to form a large coherent vortex around the TC eye (Fig. 2b). This suggests steadiness in the ocean response within the (x, y) coordinates (Geisler, 1970). To best exploit the spatiotemporal information embedded in float data, we used objective mapping (R. E. Davis, 1985; Le Traon et al., 1998) with a Gaussian decorrelation scale of 150 km to horizontally interpolate measurements $\mathbf{u}_{surf}$, $\mathbf{u}_{mean}$, T, and S. The signal-to-noise ratio for objective mapping was set to 10,

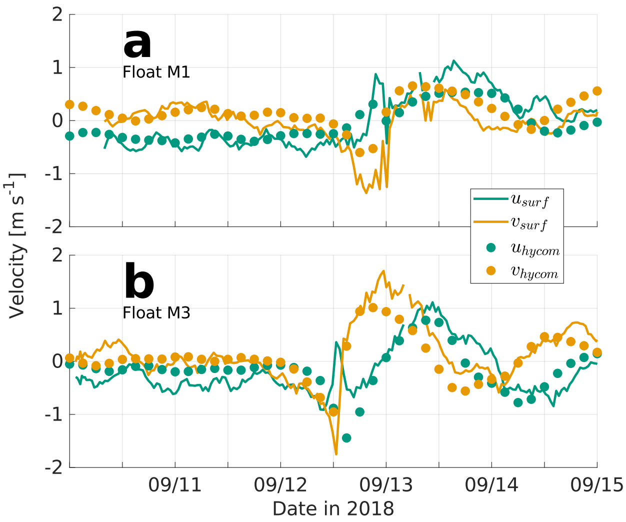

Figure 3. (**a**) and (**b**) compare measurements $\mathbf{u}_{surf}$ by floats M1 and M3 (lines) to ML velocity data $\mathbf{u}_{hycom}$ from the ocean component of our coupled 3D model (circles) $\mathbf{u}_{hycom}$ is taken from fixed model locations representative of each float's track.

and areas where the estimated mean square error of interpolated fields is greater than 7.5% of signal variance have been masked out in plots.

To reconstruct 3D patterns in T and S, we stacked 2D maps at 5 meter intervals and produced the 3D fields $T^*(x,y,z)$ and $S^*(x,y,z)$. Here, the star * denotes objectively mapped variables. Although vertical variations in u, v were not measured directly, we use differences between $\mathbf{u}^*_{surf}$ and $\mathbf{u}^*_{mean}$ to separate the ML flow from the less energetic ocean below. More precisely, we assume that depth-dependence at each location (x,y) is given by

$$\mathbf{u}^*(x,y,z) = \begin{cases} \mathbf{u}^*_{surf} & z \geq -h \\ \mathbf{u}^*_{surf} + \left\langle \frac{\partial \mathbf{u}}{\partial z} \right\rangle (z-h) & -h > z > -h-l \\ \mathbf{u}^*_{surf} + \left\langle \frac{\partial \mathbf{u}}{\partial z} \right\rangle l & -h-l \geq z \geq -H. \end{cases} \tag{1}$$

The piecewise function (1) includes two layers of depth-constant velocity and a sheared transition layer between them. Flow in the uppermost layer, which spans the depth of the ML $-h < z \leq 0$, is given by $\mathbf{u}^*_{surf}$. Here, h is defined as the depth at which T^* is 0.2 °C colder than it is at 20 m depth. Below $z = -h$, we assume a transition layer of thickness $l = 30$ m (Johnston & Rudnick, 2009) and constant shear

$$\left\langle \frac{\partial \mathbf{u}}{\partial z} \right\rangle = 2H \frac{\mathbf{u}^*_{surf} - \mathbf{u}^*_{mean}}{[l^2 + 2l(H-l-h)]}. \tag{2}$$

This transition layer of increased stratification is set by the vertical penetration of wind-driven turbulent momentum, which determines the depth at which $\mathbf{u}$ no longer behaves like a slab (Turner & Kraus, 1967; Pollard et al., 1973). Lastly, the third and deepest layer extends down to $H = 180$ m and has velocities $\mathbf{u}^*_{surf} + \left\langle \frac{\partial \mathbf{u}}{\partial z} \right\rangle l$. This construction makes the depth-mean of $\mathbf{u}^*$ between $z = 0$ and $z = -H$ strictly equal to $\mathbf{u}^*_{mean}$.

Concentrating $\left\langle \frac{\partial \mathbf{u}}{\partial z} \right\rangle$ within a transition layer captures some of the main features of wind-forced currents. Thus, equations (1) and (2) yield an idealized 3D velocity field constrained by float velocity estimates and previous knowledge of the baroclinic response to TC forcing. However, it should be noted that high baroclinic modes that cannot be represented by (1). Likewise, small-scale vertical shear associated with turbulence is not resolved here. Instead, the characteristics of such fine scale processes will be described in Section 4 using vertical profiles of T and S.

To finalize the reconstruction of 3D flows beneath Mangkhut from float measurements, we impose a condition of adiabatic continuity to obtain $\frac{\partial w^*}{\partial z} = -\frac{\partial u^*}{\partial x} - \frac{\partial v^*}{\partial y}$. Furthermore, we assume a rigid lid so that $w^*(z=0)$ vanishes and $w^*(z<0)$ at a given point (x, y) is

$$w^*(z) = \int_0^z \left(\frac{\partial u^*}{\partial x} + \frac{\partial v^*}{\partial y} \right) dz'. \tag{3}$$

Before showing the interpolated fields T^*, S^*, u^*, v^*, w^*, we must emphasize that (1) the decorrelation scale $L = 150$ km suppresses high-frequency features in the observations, and (2) some caution is warranted when interpreting results near the edge of the objective maps.

2.2 Thorpe scale estimates of turbulence

Vertical profiles of T and S taken at 1 Hz (vertical resolution ~ 0.1 m) were used to compute in situ density ρ. These allowed to derive Thorpe scale estimates (Thorpe, 1977) of the turbulent dissipation rate ε and diffusivity κ within unstable overturns where $\frac{\partial \rho}{\partial z} > 0$. This method computes the vertical displacements d' necessary to reorder water parcels within a given overturn such that ρ increases with depth. This defines the Thorpe scale $L_{Ti} = \sqrt{\langle d'^2 \rangle_i}$, where the brackets indicate averaging within an overturn i. Ultimately, ε was calculated as

$$\varepsilon_i = 0.64 L_{Ti}^2 \langle N \rangle_i^3. \tag{4}$$

Here, $\langle N \rangle_i$ is the mean buoyancy frequency calculated from the sorted profile of ρ. Next, we used the relation in Osborn (1980) to compute $\kappa_i = 0.2 \frac{\varepsilon_i}{\tilde{N}^2}$. Here, $\tilde{N}^2$ is the background squared buoyancy frequency averaged from multiple ordered profiles of ρ. With this, ε and κ were indirectly estimated for all overturns whose $L_{Ti} > 5$ m. This allows us to estimate the downward turbulent heat flux across overturns as (5). There, the constants are $\rho_0 = 1024$ kg m^{-3} and $C_p = 4000$ J kg^{-1} °C^{-1}. More details on the implementation, assumptions, and limitations of the Thorpe scale method can be found in A. Thompson et al. (2007); Mater et al. (2015); Scotti (2015).

$$J_{qi} = \rho_0 C_p \kappa_i \langle \frac{\partial T}{\partial z} \rangle_i \tag{5}$$

3 Mixed layer theory

In this section, we review the mechanisms of NIW generation by TCs and formulate ML dynamics using vorticity ($\zeta = \nabla \times \bar{\mathbf{u}}$) and divergence ($\Gamma = \nabla \cdot \bar{\mathbf{u}}$) instead of depth-averaged ML currents $\bar{\mathbf{u}}$. As shown below, this simple change of variables leads to a set of ordinary differential equations describing inertial pumping, which must be otherwise described using partial differential equations (Gill, 1984). Lastly, numerical solutions of the (ζ, Γ, h) model are used to compare NIW generation under fast- and slow-moving TCs.

The dynamic response of $\bar{\mathbf{u}} = (\bar{u}, \bar{v})$ to a wind stress $[\tau = (\tau_x, \tau_y)]$ in a ML of thickness h can be described using the linear slab model in (6) and (7). Solutions to these equations, first used by Pollard & Millard (1970) to explain in-situ measurements, feature a slowly-varying component that approximates an Ekman balance and inertial oscillations whose amplitude decays at a rate r. In order to resolve vertical velocities $\frac{\partial h}{\partial t}$ at the ML base, we couple (6) and (7) to the continuity equation (8). Here, $W_e \geq 0$ is an entrainment rate used to represent ML deepening caused by turbulent mixing (Price, 1981).

$$\frac{\partial \bar{u}}{\partial t} = f\bar{v} + \frac{\tau_x}{\rho_0 h} - r\bar{u} \tag{6}$$

$$\frac{\partial \bar{v}}{\partial t} = -f\bar{u} + \frac{\tau_y}{\rho_0 h} - r\bar{v} \tag{7}$$

$$\frac{\partial h}{\partial t} + h\nabla \cdot \bar{\mathbf{u}} = W_e \tag{8}$$

Because our focus here is on NIW generation, (6)-(8) exclude forces that make negligible or secondary contributions to $\frac{\partial h}{\partial t}$. For example, barotropic flows develop in TC wakes (Shay & Chang, 1997), but the horizontal pressure gradients that drive them scale to make a negligible contribution to $\frac{\partial h}{\partial t}$ given the large horizontal scale of TCs (Geisler, 1970; Gill, 1984; D'Asaro, 1989). Similarly, nonlinear solutions of $\frac{\partial h}{\partial t}$ under TCs (Price, 1981) show good agreement with the linear case solved by Geisler (1970), so advective terms $\bar{\mathbf{u}} \cdot \nabla \bar{\mathbf{u}}$ and $\bar{\mathbf{u}} \cdot \nabla h$ can be dropped.

When the mixed layer oscillates at frequencies slightly greater than f, periodic pumping of the ML base allows downward momentum transfer by NIWs (Price, 1983; Gill, 1984). In the past, the baroclinic ocean response to TCs has been studied by coupling contiguous layers of increasing density through pressure gradients produced by interfacial displacements (Geisler, 1970; Price, 1981, 1983). Instead, (6) and (7) use the empirical damping rate r to parameterize the downward propagation of internal waves, dissipation, and nonlinearities that drive Eulerian momentum decay in the ML (Pollard & Millard, 1970; D'Asaro, 1985).

In the mid latitudes, reduction of horizontal scales that enhances these fluxes largely depends on gradients in the mesoscale and planetary vorticity (Kunze, 1985; D'Asaro, 1989; Johnston et al., 2016; Asselin & Young, 2020). In contrast, the spatial structure of TC winds imprints sharp gradients on upper ocean currents and thus allows for immediate generation of NIWs (D'Asaro, 1989). To emphasize this point, we now consider the ML response to TC forcing not in terms of $\bar{u}$ and $\bar{v}$, but their spatial gradient.

3.1 Dynamics of wind-forced gradients in the upper ocean

Below, we manipulate (6)-(8) to isolate the components that contribute to $\frac{\partial h}{\partial t}$ and thus generate NIWs. To do this, we calculate $\frac{\partial \zeta}{\partial t} = \nabla \times \frac{\partial \bar{\mathbf{u}}}{\partial t}$ and study its relation to $\frac{\partial \Gamma}{\partial t} = \nabla \cdot \frac{\partial \bar{\mathbf{u}}}{\partial t}$. Past studies have used ζ and Γ as a basis in fluid dynamical models (Névir & Sommer, 2009), and the relevance of these variables to NIW generation has been noted by Gill (1984); Nagai et al. (2015); Whitt & Thomas (2015). Taking the curl and divergence of (6) and (7) thus yields an alternative representation of ML dynamics

$$\frac{\partial \zeta}{\partial t} = -f\Gamma + \frac{1}{\rho_0 h}\left(\nabla \times \tau - \frac{\tau}{h} \times \nabla h\right) - r\zeta \tag{9}$$

$$\frac{\partial \Gamma}{\partial t} = f\zeta + \frac{1}{\rho_0 h}\left(\nabla \cdot \tau - \frac{\tau}{h} \cdot \nabla h\right) - r\Gamma \tag{10}$$

$$\frac{\partial h}{\partial t} + h\Gamma = W_e. \tag{11}$$

This formalism does not explicitly include information about the magnitude and direction of currents. Instead, it uses the physical principles in (6)-(8) to resolve spatiotemporal patterns in $\frac{\partial h}{\partial t}$ that ultimately generate internal waves. It is worth noting that, under axial-symmetric storms, $\nabla \cdot \tau$ and $\nabla \times \tau$ are fully determined by radial and tangential winds respectively. Thus, (9) and (10) show how these separate components of τ directly drive orthogonal but coupled modes of motion Γ and ζ in upper ocean flow.

In TC wakes, once winds cease to play a dominant role and the ML evolves freely, our diagnostic model (9)-(11) yields the three term balance in (12) and (13). This linear system of equations, a damped harmonic oscillator, produces inertial cycles in ζ and Γ with an exponential decay rate r. Inertial pumping arises directly from these cycles, which are simply a consequence of clockwise rotation in $\bar{\mathbf{u}}$.

$$\frac{\partial \zeta}{\partial t} = -f\Gamma - r\zeta \tag{12}$$

$$\frac{\partial \Gamma}{\partial t} = f\zeta - r\Gamma. \tag{13}$$

To visualize how (12) and (13) is an explicit statement of inertial pumping, we follow Gill (1984) and set $\tau = W_e = r = 0$ to consider the evolution starting at time $t = t_i$ with $(\zeta_i, \Gamma_i) = (c_i, 0)$ where $c_i > 0$. As illustrated in Fig. 4, (12) and (13) imply that inertial rotation of current vectors transfers momentum from ζ into Γ, and from Γ into $-\zeta$ at time intervals $\frac{\pi}{2f}$. Quadrature between ζ and Γ in this oscillatory mode means that NIW crests (troughs) must be surrounded by anticyclonic (cyclonic) inertial currents (Fig. 4). This correspondence between ζ and ML displacements has the important implication that wind-driven, inertially-oscillating ML vortices and corresponding vertical displacements in the ocean interior can be sometimes mistaken for quasigeostrophic eddies.

3.2 Relating upwelling and NIW generation to TC winds

When winds act on the ocean surface, momentum imparted by τ drives both mean and turbulent flows. Initially, the horizontal velocity $\bar{\mathbf{u}}$ accelerates in the direction of τ while turbulence helps distribute momentum vertically and deepen the ML. Later on, $\bar{\mathbf{u}}$ is steered in clockwise rotation by $f > 0$ such that τ become misaligned. After half an inertial period of constant forcing τ, the response $\bar{\mathbf{u}}$ approaches an Ekman balance where $(\bar{u}, \bar{v}) \sim \frac{1}{f\rho_0 h}(\tau_y, -\tau_x)$ is orthogonal to τ (Ekman, 1905) and ML deepening stops (Pollard et al., 1973).

Setting $\nabla h = 0$ in (9)-(11), we may write Ekman's balance as $(\zeta, \Gamma) \sim \frac{1}{f\rho_0 h}(-\nabla\cdot\tau, \nabla\times\tau)$, so that Γ becomes sustained by $\nabla\times\tau$. However, notice that $\nabla\times\tau$ does not directly drive the evolution of Γ in (10). Instead, $\frac{\partial \zeta}{\partial t}$ and $\frac{\partial \Gamma}{\partial t}$ under τ will initially mirror patterns in $\nabla\times\tau$ and $\nabla\cdot\tau$ respectively. It is only later that the clockwise steering of currents by $f > 0$ gradually links $\nabla \times \tau$ to Γ and produces upwelling (Fig. 4).

The rate at which f steers $\bar{\mathbf{u}}$ away from the direction of τ gives rise to qualitative differences between the ocean response to fast-moving and slow-moving storms. Using a two-layer model, Geisler (1970) showed that energy transfer into NIWs decreases with the ratio $U_{storm}/\|\mathbf{c_g}\|$, where $\|\mathbf{c_g}\|$ is the group speed of mode-1 internal waves. At the limit where $U_{storm}/\|\mathbf{c_g}\| < 1$, Geisler's solutions predict that the momentum in $\nabla\times\tau$ is entirely used by Ekman-style upwelling with no oscillatory behavior. Nilsson (1995)

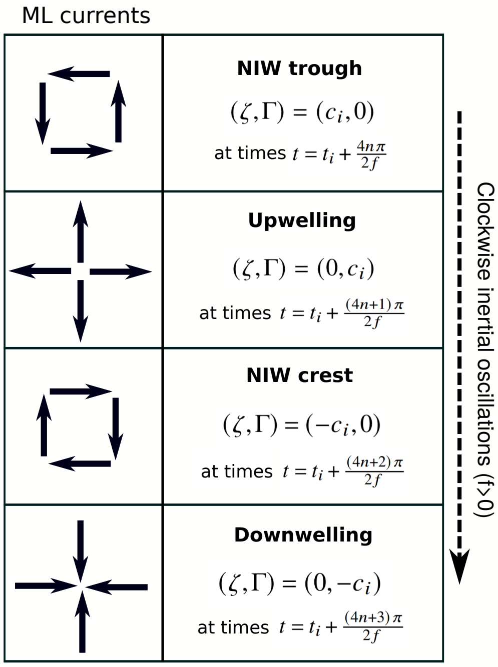

Figure 4. Successive rows illustrate the time evolution of current vectors under clockwise inertial oscillations. The left column shows schematic vews of $\mathbf{u}$ at temporal intervals $\frac{n\pi}{2f}$ $(n = 0, 1, 2, \ldots)$. Over this period, clockwise rotation of $\mathbf{u}$ by 90° fully transforms ζ into Γ, and Γ into $-\zeta$.

later used a normal mode expansion approach to find supporting results in a continuously stratified fluid.

The formalism in (9)-(11) does not explicitly represent $\mathbf{c_g}$, but instead uses r to parameterize its effects. Hence, we investigate whether this simple model of NIW generation can represent the transition between balanced and oscillatory regimes described by Geisler (1970) and Nilsson (1995). To do this, we used Euler's method to compute point solutions (setting $\nabla h = 0$) of (9)-(11) under the forcing of Gaussian vortices $\nabla \times \tau$ with standard deviations of 2 and 6 hours to represent fast- and slow-moving TCs. These vortices represent the changing direction of tangential τ inside an axisymmetric TC eye but do not include radial stresses, which are known to make only minor contributions to NIW generation (Price, 1983; Shay et al., 1989). The evolution of $(\zeta/f, \Gamma/f, h)$ from an initial condition $(0, 0, 80\text{ m})$ under both scenarios is shown in Fig. 5.

Numerical solutions of (9)-(11) in Fig. 5 exemplify the two fundamental differences noted by Geisler (1970). Firstly, notice that the greatest upwelling (maximum Γ/f) occurs at the end of the forced stage for the fast-moving case (Fig. 5b), whereas Γ/f peaks well within the slow TC's forced stage (Fig. 5c). Moreover, the net mixed layer displacement induced by the slow-moving TC is greater than for the fast-moving case (Fig. 5d). This is consistent with a greater transmission of energy into balanced motions (rather than inertial oscillations) for slowly-varying τ (Veronis, 1956; Pollard, 1970).

The second point of agreement between our simple model and Geisler (1970) relates to the amplitude of NIWs generated by fast- and slow-moving TCs . While solutions to $\frac{\partial h}{\partial t}$ have no oscillatory behavior when $\frac{U_{storm}}{\mathbf{c}_g} < 1$, damping by r in (9)-(11) regulates the fraction of momentum that enters the damped oscillator in (12) and (13) at the end of the forced stage. This is evidenced in Fig. 5 because the amplitude of NIWs

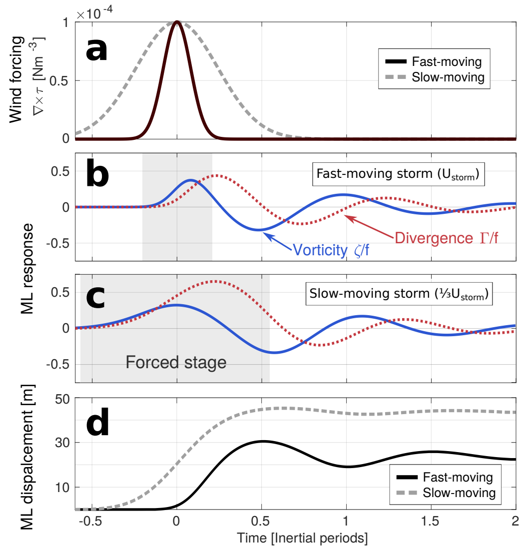

Figure 5. ML response (9)-(11) to (**a**) wind vortices representing (**b**) a fast-moving TC and (**c**) one moving at one-third the speed. (**d**) compares the mixed layer displacements $h(t_0) - h(t)$ that result from both simulations when $W_e = 0$. Gray shading in (**b**) and (**c**) marks the forced stage, which is followed by near-inertial pumping as given by (12) and (13).

generated by the slow-moving vortex is less than half that NIWs generated in fast-moving case (Fig. 5d and Figs. 3-5 in Geisler 1970).

The linear (ζ, Γ) view of ML dynamics (9)-(11) does not include any new physics absent from standard ocean models based on (u, v). Rather, it uses a simple change of variables to explain inertial pumping (Fig. 4) using ordinary differential equations rather than partial ones, as done by Gill (1984). This helps conceptualize inertial pumping and upwelling as 1D (rather than 3D) processes. Moreover, example solutions in Fig. 5 suggest that the qualitative differences between the ocean response to fast- and slow-moving storms can be recovered from simpler principles than those used by Geisler (1970) and Nilsson (1995). In the next section, we use float measurements and output from WRF-HYCOM coupled simulations of Mangkhut to demonstrate the relevance of (9)-(11) in describing NIW generation under fast-moving TCs.

4 Upper ocean dynamics beneath Mangkhut

We now turn our attention towards model output and observations of upper ocean dynamics beneath Super Typhoon Mangkhut. First, we present evidence supporting the validity of sampling and interpolation schemes described in Section 2. Second, the evolution of ζ and Γ in our observations is compared to the linear model (9)-(10) while T and S data confirm the generation of a large amplitude NIW as predicted by (11). Estimates of Γ and the corresponding w^* (3) are shown to be in agreement with observed isothermal displacements and NIW generation behind Mangkhut. The role of turbulent mixing in changing h is discussed briefly but further details are given in the next section.

Hovmöller diagrams of $\bar{\mathbf{u}}$ and $(\zeta, \Gamma)/f$ in Figs. 6a,b show the ocean response to Mangkhut along 133°E in the coupled 3D model. Observational estimates $\mathbf{u}^*_{surf}$ and $\mathbf{u}^*_{mean}$ are shown with their corresponding $(\zeta, \Gamma)/f$ fields in Fig. 7. To compare model output and observations, Fig. 6c shows a time series of the modelled $(\zeta, \Gamma)/f$ averaged between 14 and

14.5°N (solid lines) and estimates ζ^*_{surf}/f along $y = 0$ (dashed lines). To help with comparisons, the dashed rectangle in Fig. 6a represents the area shown in Fig. 7 and other visualizations of interpolated float measurements.

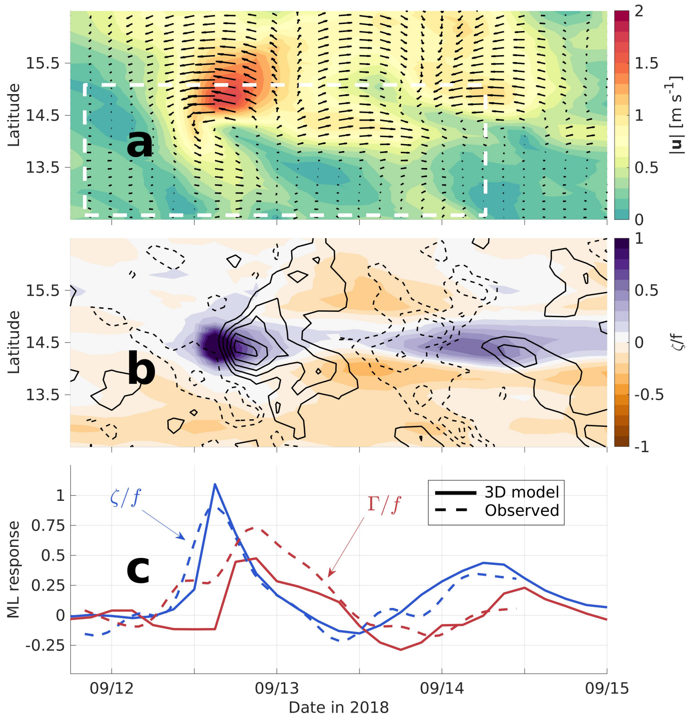

Figure 6. Time-latitude sections of the ML flow along 133°E in coupled 3D simulations of Mangkhut. Arrows and color shading in (**a**) show the direction and magnitude of $\bar{\mathbf{u}}$. Color shading in (**b**) shows ζ/f, while black contours denote $\Gamma/f \neq 0$ at 0.1 intervals (negative dashed). (**c**) compares model output of $(\zeta, \Gamma)/f$ averaged between 14 and 14.5°N (solid lines) to observational estimates made using $\mathbf{u}^*_{surf}$ along $y = 0$ (dashed lines). The dashed rectangle in (**a**) is representative of the area shown by Fig. 2b and visualizations of interpolated data.

Quantitative agreement between ML current speeds in the model (Fig. 6a) and observations (Fig. 7a) is good, with $\|\bar{\mathbf{u}}\|$ reaching $\sim$ 1 m s^{-1} on the leading edge of the TC eye and $\sim$ 2 m s^{-1} on the right side of the TC track. Spatiotemporal patterns in $\mathbf{u}^*_{surf}$ and $\mathbf{u}^*_{mean}$ (Fig. 7a,b) are qualitatively similar to each other, suggesting that windage and wave motion do not significantly impact smoothed patterns in $\mathbf{u}^*_{surf}$.

The greatest difference between modelled and observational velocity estimates is that HYCOM produced $u \sim 1$ m s^{-1} at $t \sim 1/2$ inertial period (September 13 in Fig. 6a) but this features is missing in observations (Fig. 7a). This may be due to inaccuracies in float measurements or enhanced damping of inertial oscillations by background conditions not considered in HYCOM (Guan et al., 2014; Whitt & Thomas, 2015). Despite this difference, general agreement between observations and model output suggests that the sampling and interpolation scheme described in Section 2 appropriately captures the primary characteristics of upper ocean response to TC forcing.

In both the observational records and the model, ζ/f peaked during TC passage and later evolved in quadrature with Γ/f as the amplitude of oscillations decayed (Figs. 6b,c, 7c,d). Ocean currents near the TC eye were dominated by a vertical core with $\zeta_{hycom}/f \sim$ 1, $\zeta^*_{surf}/f \sim 1$ and $\zeta^*_{mean}/f \sim 0.4$ (color shading in Figs. 6b, 7c,d). Wind-forced vortices later evolved into maxima of $\Gamma_{hycom}/f \sim 0.5$, $\Gamma^*_{surf}/f \sim 0.7$ and $\Gamma^*_{mean}/f \sim 0.4$ near $x = 150$ km (black contours in Figs. 6b, 7c,d). Local minima in ζ/f trail the TC around x $=$450 km. As described in Section 3, vertical currents near the TC eye correspond to the ocean's immediate response to $\nabla \times \tau$ (Eqn. 9), while subsequent coupled oscillations in ζ/f and Γ/f result from the clockwise rotation of current vectors (Figs. 4, 5).

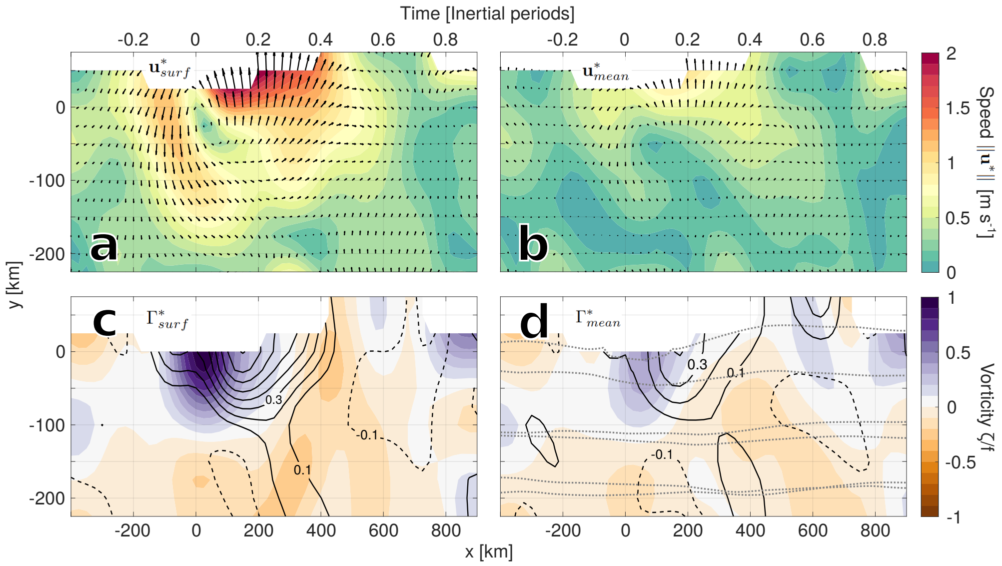

Figure 7. Two-dimensional maps of $\mathbf{u}^*_{surf}$ (left) and $\mathbf{u}^*_{mean}$ (right) are viewed through their speed and direction (**a**, **b**) and their ζ, Γ components (**c**, **d**). Color in **c** and **d** shows ζ^*_{surf}/f and ζ^*_{mean} respectively, while Γ^*_{surf}/f and Γ^*_{mean}/f are shown in black contours. Contours are continuous for upwelling-favorable values $\Gamma/f > 0$, while dashed contours show $\Gamma/f < 0$. Dotted lines (**d**) show the float tracks.

Overall, good agreement is seen between (ζ, Γ) in the 3D model and observations (Fig. 6c). However, estimates of Γ/f differ significantly near the leading edge of the TC eye, where $\Gamma^*_{surf}/f \sim 0.25$ but $\Gamma_{hycom}/f \sim -0.1$. It is unclear whether this difference results from imperfect sampling and interpolation of float data, preexisting ocean conditions missing from the 3D model, or inaccuracies in the modelled surface winds.

With the validity of our observational technique supported by model output and by similarities between $\mathbf{u}^*_{surf}$ and $\mathbf{u}^*_{mean}$, we now test whether the simple model in (9) and (10) can reproduce observed cycles in $(\zeta^*_{surf}, \Gamma^*_{surf})/f$. Moreover, we use $T*(x, y, z)$ to test equation (11) relating ML dynamics and NIW generation. To do so, we take interpolated float data along $y = 0$ and compare observations to numerical solutions of (9)-(11) under idealized TC forcing with a damping rate $r = 0.5f$ (Fig. 8).

Atmospheric forcing $\nabla\times\tau$ in Fig. 8 corresponds to the reversal of tangential wind between opposite sides of the TC eyewall. The magnitude of $\nabla\times\tau$ used here agrees with the mean wind stress curl inside the TC eye ($\frac{|\tau_{\mathbf{max}}|}{\mathrm{MWR}} = 2.24\times10^{-4}$ N m^{-3}, dashed line). Here, $MWR = 40$ km is the radius of maximum wind, while $|\tau_{max}| = C_D \rho_{air} |U_{10}|^2$ was calculated using $U_{10} = 70$ m s^{-1} (Fig. 1), $\rho_{air} = 1.22$ kg m^{-3}, and $C_D = 1.5 \times 10^{-3}$ (Zweers et al., 2010).

The magnitude of convergent stresses $\nabla\cdot\tau < 0$ is set to be artificially low in these simulations (Fig. 8a). Although $\|\nabla \cdot \tau\| \sim \|\nabla \times \tau\|$ in the 3D atmospheric model, a great deal of the momentum that $\|\nabla{\cdot}\tau\|$ imparts on Γ is rapidly countered by nonlinear effects and thus does not contribute significantly to NIW generation in the TC wake (Price, 1983). Lastly, it should be noted that forcing in Fig. 8a ignores the gradual weakening of τ far from the eyewall, where $\nabla \times \tau < 0$ and $\nabla \cdot \tau > 0$.

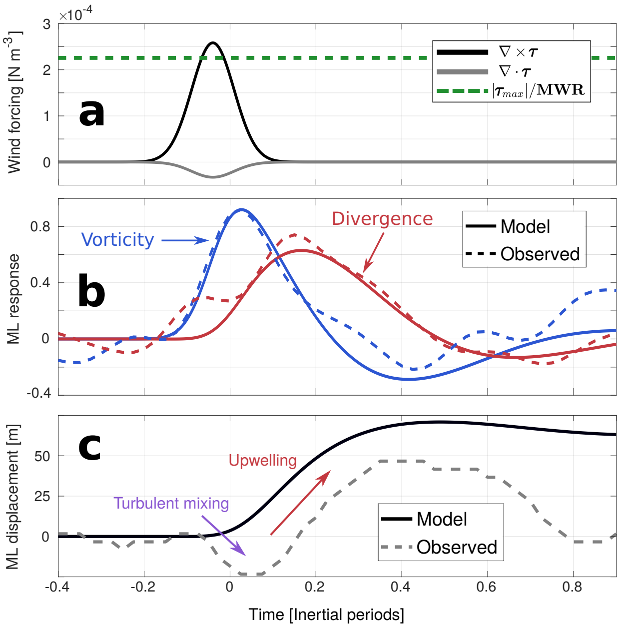

Figure 8. ML response to idealized TC-like atmospheric forcing. Numerical solutions of (9)-(11) setting $W_e = \nabla h = 0$ were obtained using the wind forcing terms in panel **a**. (**b**) compares solutions to estimates of ζ/f (blue) and Γ/f (red) made using $\mathbf{u}^*_{surf}$ (Fig. 7c) along y=0 km. Linear solutions of $h(t)$ (**c**, solid line) agree with observed displacements of the 27°C isotherm (dashed line).

Agreement between linear solutions and observations in Fig. 8 confirms that clockwise rotation of $\bar{\mathbf{u}}$ (Fig. 2b) transformed the wind-forced ζ/f into Γ/f near the end of the forced stage. Momentum in Γ/f was later transferred to an inertial anticyclone $\zeta/f < 0$ and the cycle continued as shown schematically in Fig. 4.

Observations show that the 27°C isotherm deepened by ∼25 m under the TC eye before it shoaled by 75 m as predicted by linear theory (Fig. 8c). Initial deepening may be partially explained by turbulent mixing, evidenced by Thorpe scale estimates $\kappa \sim 10^-1$ m^{2}s^{-1} near $x = 0$ km (Fig. 9b). Agreement between the modelled $\frac{\partial h}{\partial t}$ and observed displacements of the 27°C isotherm behind the TC suggests that measurements Γ^*_{surf} are accurate there (Fig. 8c). This implies that upwelling in the wake of Mangkhut resulted from the near-inertial coupling of ζ/f and Γ/f, marking the generation of a large amplitude NIW. Moreover, the modelled Γ/f agrees well with Γ^*_{surf} for all $t > 0$ (Fig. 8b). Nonetheless, Γ^*_{surf} failed to capture downwelling necessary to displace h after $t \approx$ 0.6 inertial periods (Fig. 8c).

Profiles of w^* and u^* in Fig. 9a reveal the structure of upwelling in the wake of Mangkhut. There, w^* reaches 8 m h^{-1} and explains isothermal displacements as large as 75 m around x = 350 km. T^* shows that isotherms had been lifted by ∼ 20 m after ∼0.85 inertial periods (x = 850 km, Fig. 9a). This net upwelling is crucial to the process of geostrophic adjustment (Geisler, 1970; Nilsson, 1995), and determined in (10)-(11) by the magnitude of r.

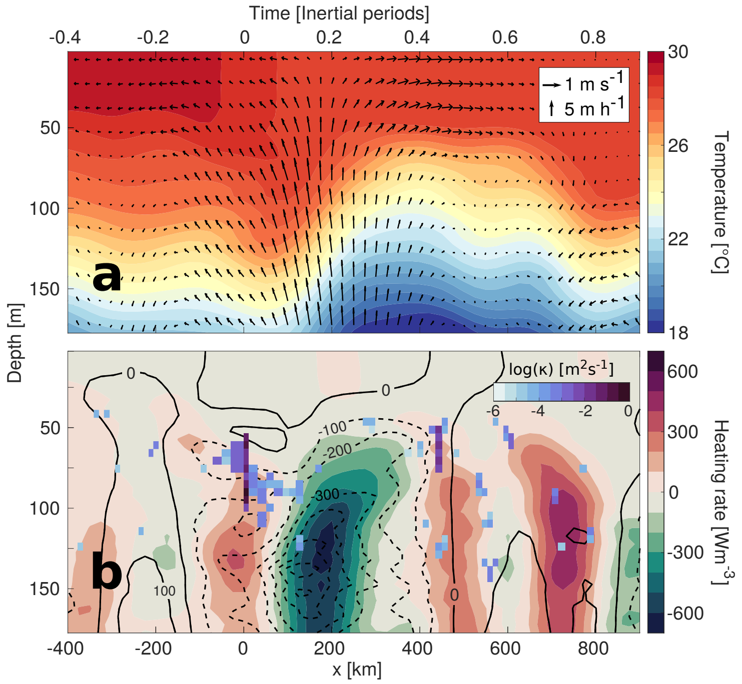

Figure 9. Vertical sections of T^* and (u^*, w^*) along y=0 (**a**) show the generation of a NIW behind Super Typhoon Mangkhut. The vertical component w^* is magnified for clarity. (**c**) shows frozen field estimates (color shading) and advective contributions (contours at 100 W m^{-3}, dashed for negative values) to the Eulerian heating rate $\frac{\partial H_c}{\partial t}$, while estimates of κ indicate the intensity of vertical mixing inferred from M3 (note the log scale).

To test the impacts of advection in setting the ocean stratification behind Mangkhut, as well as the accuracy of inferred 3D flows (Eqs. 1-3), the Eulerian heating rate $\frac{\partial H_c}{\partial t} = \rho_0 C_p \frac{\partial T^*}{\partial t}$ is calculated along $y = 0$ through two different methods (Fig. 9c). First, we used a frozen field assumption so that $\frac{\partial T^*}{\partial t} = U_{storm} \frac{\partial T^*}{\partial x}$ (color shading). Second, we used $\mathbf{u}^*$ and w^* to calculate the advective contribution $\frac{\partial T^*}{\partial t} \approx -u^* \frac{\partial T^*}{\partial x} - v^* \frac{\partial T^*}{\partial y} - w^* \frac{\partial T^*}{\partial z}$ (black contours). Both expressions ignore mixing, which may be represented by the term $-\frac{\partial J_q}{\partial z}$.

Areas of agreement between both estimates of $\frac{\partial H_c}{\partial t}$ (color shading and black contours in Fig. 9b) suggest that heat transfer was locally dominated by the vertical advection term $w^* \frac{\partial T^*}{\partial z}$ and that the approximation w^* is adequate. Similarities are particularly good near $x = 180$ km, where upwelling caused $\frac{\partial H_c}{\partial t} \sim$ -500 W m^{-3}. In contrast, downwelling velocities w^* were underestimated near $x = 700$ km and the advective estimate failed to produce the $\frac{\partial H_c}{\partial t} > 400$ W m^{-3} inferred from T data.

Advective estimates of $\frac{\partial H_c}{\partial t}$ mistakenly predict cooling below 75 m depth around $x = 0$, where T^* shows heating rates as high as 300 W m^{-3} (color shading). Disagreement between observed heating and advective estimates below the TC eye may be explained by a possible bias in Γ^*_{surf} (Fig. 6c) but also by vigorous mixing. Thorpe scale estimates $\kappa \sim 10^{-1}$ m^2 s^{-1} near $x = 0$ (Fig. 9b) reveal areas where the corresponding turbulent heatflux $J_q \sim 4000$ W m^{-2} could invalidate the assumption that $\frac{\partial H_c}{\partial t}$ was dominated by advection.

While variations in the ML flow are dominated by near-inertial oscillations (Fig. 8), $\frac{\partial H_c}{\partial t}$ shows the signature of super-inertial motions (Fig. 9b). Horizontal sections of $\zeta^*/f, \Gamma^*/f$, and $N^* = \sqrt{-\frac{g}{\rho_0}\frac{\partial \rho^*}{\partial z}}$ at 160 m depth (Fig. 10) feature nearly parallel, periodic stripes that move away from the storm track towards $y < 0$. Dashed black lines in Fig. 10 help identify this apparent propagation corresponding to a cross-track phase speed ~ 3.1 m s^{-1}. While ζ^*/f and Γ^*/f are linked by the rotation of current vectors (Fig. 4), Γ^* and N^* are linked by isopycnal displacement and stretching. Therefore, these three variables offer complementary views of internal wave phase propagation.

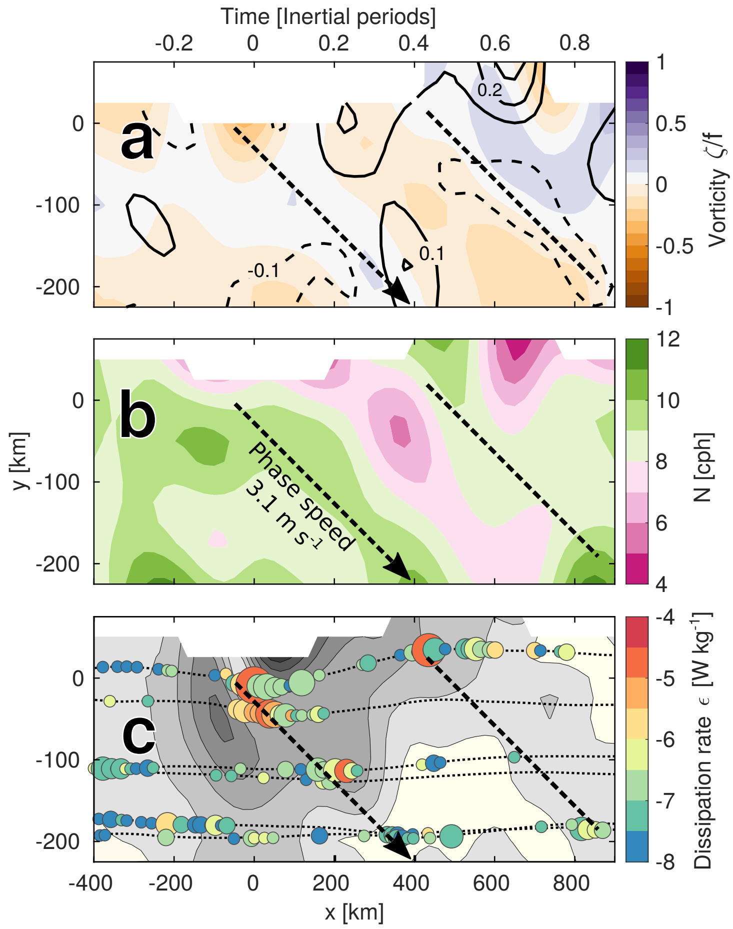

Figure 10. Horizontal sections of ζ^*, Γ^* (**a**), and N^* (**b**) at 160 m. The color of circles in panel **c** show depth-averaged estimates of ε, while their size indicates the height of overturns (range is between 5 and 25 m). Gray shading in (**c**) shows $\|\mathbf{u}^*_{surf} - \mathbf{u}^*_{mean}\|$ as a proxy for vertical shear at the mixed layer base. Thin, dotted lines denote individual float tracks. Note scales differ in x and y.

Color shading in Fig. 10c shows the magnitude $\|\mathbf{u}^*_{surf} - \mathbf{u}^*_{mean}\|$ as a proxy for vertical shear below the ML. As evidence of areas of shear instability, Thorpe scale estimates ε are shown with colored circles (Fig. 10c). Both the greatest ε and the greatest density of overturns appear within 100 km of the TC eye. Ahead of Mangkhut, overturns with $\varepsilon < 10^{-7}$ W kg^{-1} were sampled at nearly equidistant locations by floats M3, M6, and M0. Conversely, overturns in the TC wake appeared more sporadically and clustered around a few locations, but with most values of ε ranging between $10^{-7.5}$ and 10^{-6} W kg^{-1}.

5 Upper ocean thermodynamics beneath Mangkhut

5.1 Mixed layer deepening and turbulent entrainment

Space-time variations in T and S under the sea surface result from 3D advection, mixing, and interactions with the atmosphere. In the case of intense, fast-moving TCs like Mangkhut, shear-driven mixing at the ML base is expected to dominate upper ocean cooling (D'Asaro, 2003; Vincent et al., 2012). This process is evidenced by float measurements of T averaged between 0.5 and 1.5 m depth (Fig. 11a), which show a generalized cooling trend during storm passage. In particular, 1-m binned profiles of T, S and potential density (σ_θ) from float M3 show a clear, gradual deepening of the ML base between $x = -250$ km and the TC eye (Figs. 11b-d).

Successive float profiles in Figs. 11b-d show decreases in SST but increases in both sea surface salinity (SSS) and σ_0 as the ML deepened. This corresponds to entrainment of cold, salty water from below. As further evidence of the vigorous turbulence that transformed ocean thermodynamics beneath Mangkhut, vertical profiles of σ_0 feature $\sim$10 m-tall regions with unstable stratification (i.e. $\frac{\partial \sigma_0}{\partial z} > 0$, Fig. 11d). Thorpe scale estimates in Figs. 9b and 10c indicate the contribution of these density overturns to ocean turbulence. Using the values $\kappa \sim 0.1$ m^2 s^{-1} and $\frac{\partial T}{\partial z} \sim 0.01$ °C hr^{-1}, the turbulent heat flux inferred by float M3 near $x = 0$ km is $J_q \sim 4000$ W m^{-2}. For a ML with $h = 40$ m, this corresponds to an SST cooling rate $\mathcal{O}(-0.1)$ °C hr^{-1}, consistent with observations in Fig. 11a.

After storm passage, SSS (SST) had increased (decreased) for all floats (Figs. 11a, 12a), indicating widespread mixing of the upper ocean beneath Mangkhut. The influence of precipitation is also shown in Fig. 12a, as floats M5, M6 and M7 sampled sharp decreases in SSS between $x = -250$ and $x = -150$ km. To examine the impacts of rainfall in near-surface T and S, we interpolated data from the Integrated Multi-Satellite Retrievals for Global Precipitation Measurement (IMERG, Huffman et al. (2015)) onto the times and locations of float measurements. Estimated hourly rates of precipitation (size of circles) and cumulative rainfall integrated since $x = -400$ km (color) show that all floats experienced considerable precipitation (Fig. 12b). However, and despite encountering more rainfall than any other floats, M1 and M3's timeseries of SSS do not feature decreases attributable to precipitation (Fig. 12b).

In order for precipitation to impact SSS data, surface rain layers must form and remain stable for long enough (> 30 minutes) to be sampled by floats. However, this is only possible when buoyancy production by rainfall is greater than buoyancy mixing rates that diffuse salinity gradients (E. J. Thompson et al., 2019). Namely, there exist wind speed thresholds for which freshwater inputs are mixed into the ML more rapidly than observations can resolve. This leads to the interpretation that floats M1 and M3 did not measure significant SSS freshening (Fig. 12a) due to increased wind speeds and corresponding turbulence near the TC track (Price, 1981).

Successive profiles of T and S retrieved by float M7 (Fig. 13) detail the process of rain layer formation and their subsequent destruction via mixing. At the beginning of this sequence (Figs. 13a,b), consecutive float profiles ranging from $x = -246$ to $x = 0$ km show a well-mixed upper ocean with no vertical gradients in T or S. Later on (Figs. 13c,d), a layer of water with low T and S formed in the upper 5 m around $x = -140$ km (black line) but was gradually mixed and deepened over the following casts. This rain

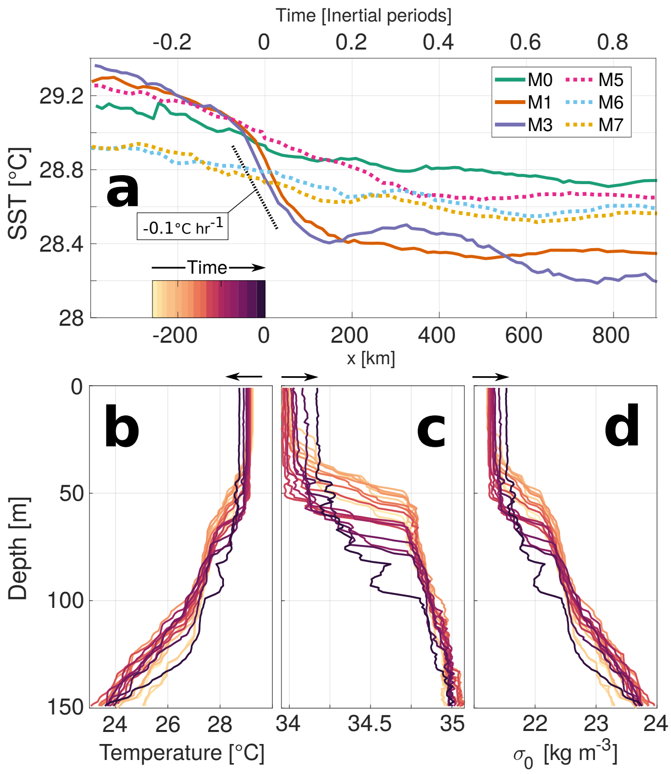

Figure 11. SST cooling by turbulent entrainment. (a) shows SST measured by all floats as a function of along-track distance x. (b), (c), and (d) are 1-m binned profiles of T, S and potential density σ_0 measured by float M3 between $x = -250$ and $x = 0$. Individual profiles shown in the lower panels are color coded by their position in x (color bar in panel a).

layer accounts for the sharp decrease in SSS measured by M7 (Fig. 12a), while the subsequent increase in SSS was consistent with mixing of cold, salty water from below. Roughly four hours (near $x = -50$ km) after its formation, there was little to no indication left that a rain layer had formed around float M7 (Figs. 13e,f).

Consistent with Thorpe scale estimates (Fig. 9b), $T^*(x, y)$ and $S^*(x, y)$ in Fig. 14 suggest that maximum mixing rates occurred within 100 km of the TC eye. Anomalies in T^* and S^* are asymmetric around the TC track, in agreement with greater windwork (Chang & Anthes, 1978; Price, 1981) and current speeds for $y > 0$ (Figs. 6a, 7a,b). Although floats preferentially sampled the left side of the storm and interpolated fields can become unreliable beyond the edges of our sampling area, measurements from floats M1 and M3 offer nearly symmetric coverage of near-surface conditions within 50 km of the storm track (Fig. 2b). SST cooling and SSS changes measured by M3 were consistently greater than for M1 (Figs. 11a, 12a), supporting the rightward bias in Fig. 14a. Overall, changes in ML T and S under Mangkhut are fully consistent with shear-driven entrainment of cold, salty waters across the ML base.

5.2 Turbulent ocean heat pump

While TC-driven turbulence is most recognized for cooling SST during the forced stage (Fig. 14a), TCs cause long-lasting impacts on upper ocean thermodynamics (Johnston et al., 2020). Many studies have explored the long-term consequences of TC-driven mixing and its potential contribution to shape tropical ocean circulation (K. Emanuel,

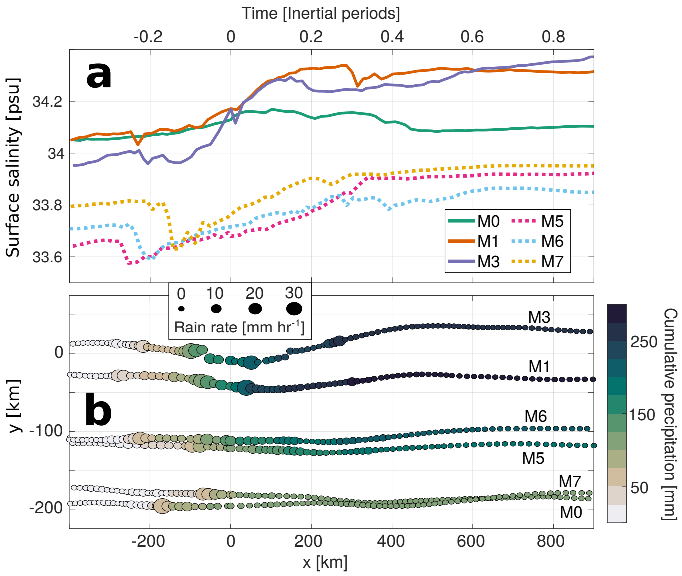

Figure 12. Combined effects of mixing and rainfall on SSS. (a) shows S averaged in the upper 5 m along float tracks. IMERG data show rain rates and cumulative precipitation along float trajectories (**b**).

2001; Sriver & Huber, 2007; Mei et al., 2013). However, quantifying the buoyancy and heat gained by the tropical thermocline due to TC mixing requires making assumptions about the magnitude, extent, and persistence of enhanced κ. Empirical estimates of κ beneath TCs can thus provide insight into the duration and intensity of turbulent heat fluxes thought to shape global ocean heat transport.

Changes in T-S relationships can inform about the magnitude and vertical extent of anomalous κ and other diabatic processes (Hautala et al., 1996; Alford et al., 1999; Moum et al., 2003). T-S relations in our data (Fig. 15) result from a combination of turbulence, 3D advection, and atmospheric fluxes. Fortunately, turbulence and advection can be differentiated by their characteristic effects on T-S plots (Hautala et al., 1996).

The progression of water-mass properties is measured by floats M1 and M3 throughout 200 km-long segments (Fig. 15a, colors). By comparing the time-averaged T-S properties sampled at different stages of storm passage, we may infer the processes that caused observed transformations. For example, average profiles measured by float M3 within the range $200 \leq x \leq 400$ km (dashed blue line) are compared to data from $400 \leq x \leq 600$ km (Fig. 15b, solid line).

In order to determine the effects of mixing in the transition between these two profiles in Fig. 15b, we used averaged T-S relations from 200-400 km as the initial condition in a diffusive model with constant κ

$$\frac{\partial T}{\partial t} \sim \kappa \frac{\partial^2 T}{\partial z^2} \tag{14}$$

$$\frac{\partial S}{\partial t} \sim \kappa \frac{\partial^2 S}{\partial z^2}. \tag{15}$$

Time evolution in (14) and (15) ignores 3D advection and air-sea fluxes, and can thus only approximate T-S transformations at depths for which mixing dominated $\frac{\partial T}{\partial t}$

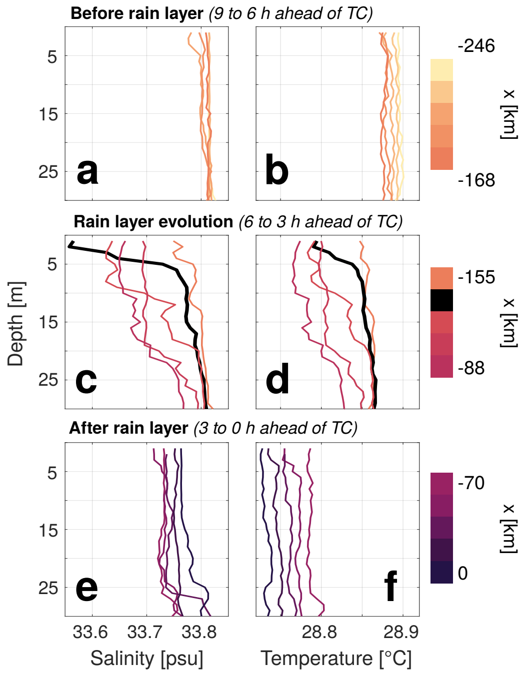

Figure 13. Evolution of a rain layer in three stages. Each row shows 5 consecutive profiles of T and S (color-coded by along-track position x) taken over a $\sim 3\,\mathrm{h}$ period. Upper panels show vertical profiles of S (**a**) and T (**b**) measured by float M7 before SSS was significantly affected by rainfall. The middle panels show a rapid decrease in near-surface salinity (**c**) and temperature (**d**). Initially, freshwater anomalies were confined to the upper 5 m (black line), but were later diffused across a greater depth (maroon lines). On panels **e** and **f**, turbulent mixing has mostly de-stratified the upper ocean.

and $\frac{\partial S}{\partial t}$. T-S properties that result from applying $\kappa = 3 \times 10^{-3}$ and 1×10^{-2} m^2 s^{-1} over 8 h (0.2 inertial periods) are shown with black dashed lines in Fig. 15b. These solutions of (14) and (15) agree well with the observed T-S changes for $\sigma_\theta < 23.2$ kg m^{-3} but fail to explain observations of greater density classes (Fig. 15b). For $\sigma_\theta > 23.5$ kg m^{-3}, S increased beyond the range of S in the initial condition. Such a transformation requires input of high-S water from elsewhere and hence cannot result from vertical mixing. Together, these features suggest that between $x = 200$ and $x = 600$ km, mixing dominated watermass transformations down to ~ 110 m depth and 3D advection had greater impacts below that.

Values $\kappa > 10^{-3}$ m^2 s^{-1} inferred from this analysis are roughly 3 to 10 times greater than the majority of Thorpe scale estimates between $x = 200$ and 600 km, whose mean value is $7.1{\times}10^{-4}$ m^2 s^{-1} (Fig. 9b). However, these estimates are not necessarily contradictory, as ocean turbulence is highly intermittent and follows a log-normal or log-skew-normal distribution (Pearson & Fox-Kemper, 2018; Cael & Mashayek, 2021). Thus, the effective κ over long periods of time (Fig. 15b) is disproportionately determined by relatively few mixing events with high κ and thousands of point measurements (Fig. 9b) are necessary to produce accurate statistics (Baker & Gibson, 1987). Therefore, estimates of κ across individual mixing events (Fig. 9b) are expected to have lower magnitudes than κ derived from analyses of watermass transformation (Fig. 15), which help infer effective or time-averaged values of κ.

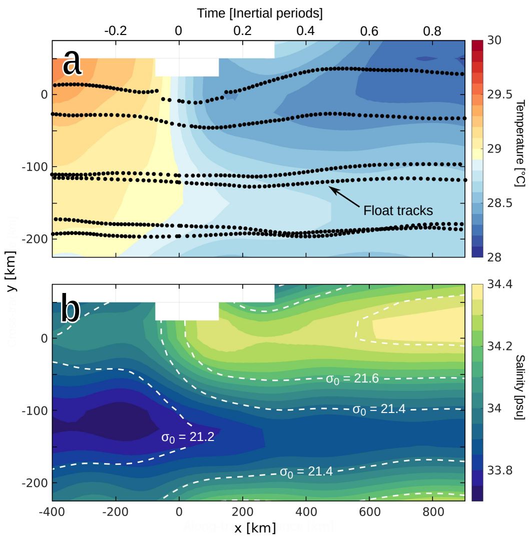

Figure 14. Plan view of T^* (**a**) and S^* (**b**) averaged over the upper 5 m. Black dots in panel **a** show the locations of each profile, while dashed contours in (**b**) show values of σ_θ in units of kg m^{-3}.

6 Discussion

The 3D ocean response to Super Typhoon Mangkhut was reconstructed and diagnosed using data from autonomous profiling floats. General agreement between interpolated fields and a 3D model (Figs. 6, 7) supports our treatment of profiler data as a viable framework to study the ocean response to TCs. Likewise, physically sensible relations between measured variables helped interpret the mechanisms driving NIW generation (Figs. 8, 9) and mixing (Figs. 10, 11, 14). Past studies have inferred the 3D structure of upper ocean features powered by TCs (Price et al., 1994; Jacob et al., 2000; Sanabia & Jayne, 2020). Nonetheless, the (ζ, Γ) framework presented in Section 3 helped to unambiguously relate observed isothermal displacements and TC forcing (Figs. 8, 9). This is particularly significant because NIW flows with $\zeta/f > 0$ and $\zeta/f < 0$ are colocated with wave troughs and crests respectively (Fig. 4) and can thus be mistaken for quasigeostrophic eddies. While the model in (9)-(11) is specific to NIW generation by winds, nonlinear dynamical models based on ζ and Γ (see for example Névir & Sommer 2009) may facilitate dynamical and conceptual insight of internal waves generated by other sources.

Float estimates of ζ and Γ are biased for $x > 500$ km, as they failed to capture $\Gamma < 0$ necessary for downwelling evidenced by T^* (Figs. 8c, 9). This is likely due to the loss of coherence by NIWs in the TC wake, since derivatives $\frac{\partial u^*}{\partial y}$ and $\frac{\partial v^*}{\partial y}$ are set by differences in measurements made more than 200 km and 12 hours apart (Figs. 2, 1). Time-dependent biases in $(\zeta^*_{surf}, \Gamma^*_{surf})/f$ affect the value $r = 0.5f$ used for numerical solutions in Fig. 8, which is considerably higher than values $\sim 0.2f$ commonly used to reproduce $\bar{\mathbf{u}}$ under extratropical storms (Pollard & Millard, 1970; D'Asaro, 1985; Alford, 2001). Even though past studies have argued that r is greater in TC wakes due to interactions with background motions (Guan et al., 2014) and the point-like nature of TC forcing (Kundu & Thomson, 1985), the value $r = 0.5f$ used here does not necessarily imply that there was enhanced ML momentum decay behind Mangkhut. A detailed analysis of NIW propagation and energetics using this dataset over longer timescales is given by Johnston et al. (2021).

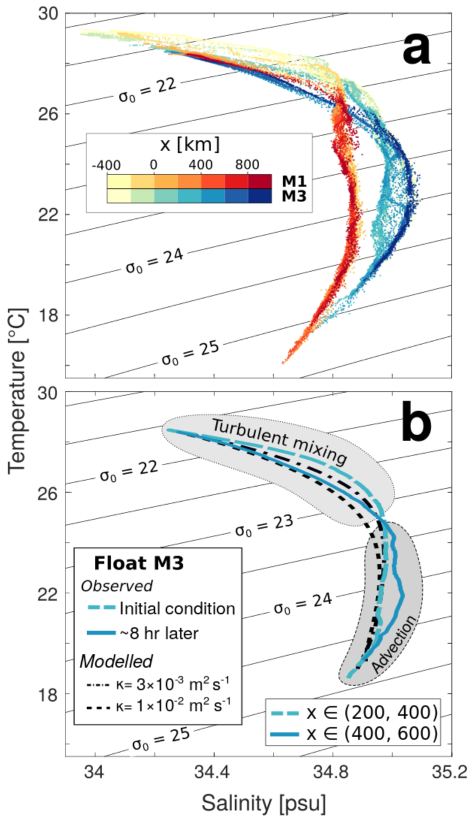

Figure 15. T-S profiles measured by floats M1 and M3 are color-coded by along-track distance in panel **a**. Mean profiles measured between 200 and 400 km (dashed line) and between 400 and 600 km (solid line) in **b** show transformations caused throughout an 8 h period. Black dashed lines show T-S properties modelled using (14) and (15) under the initial condition $x \in (200, 400)$km and different values of κ.

Vertical profiles of T and S (Figs. 11, 13) detail mixing processes that modulate storm development. Thorpe scale estimates of κ and ε (Figs. 9, 10) help assess the spatial distribution of mixing and potential impacts to air-sea interactions. While turbulent heat fluxes have been calculated directly using Lagrangian instruments (D'Asaro, 2003), the indirect approach followed here allows near real-time monitoring with potential applications in forecasting. Moreover, the watermass transformation analysis in Fig. 15 exemplifies how data from autonomous floats can be used to determine the spatial and temporal persistence TC-driven mixing. At a broader scale, this method may help understand remote mixing by TC-generated NIWs and inform better mixing parameterizations used in coupled simulations seeking to represent TC-climate interactions (Korty et al., 2008).

7 Conclusions

Formulating the linear ML dynamics (6)-(8) in terms of ζ and Γ (9)-(11) yields a direct statement of inertial pumping and explains NIW generation behind TCs. More precisely, this gradient-based view shows that the clockwise steering of currents rearranges (u, v) so that ζ evolves into Γ, and Γ into $-\zeta$ (Fig. 4). ML currents in observations and a 3D model of Mangkhut followed this pattern, which also controlled w in the TC wake (Figs. 6, 8).

Our analyses include multiple indirect descriptions of ocean mixing and its effects. Progressive changes in profiles of T and S indicate that SST cooling beneath Mangkhut was dominated by turbulent entrainment into the ML (Fig. 11, 14). This process is evidenced by density overturns that were sampled ahead and behind the TC, but most significant near the eye (Fig. 10). There, Thorpe scale estimates suggest values as high as $\kappa \sim 10^{-1}$ m^2 s^{-1}, which correspond to heat fluxes $J_q \sim 4 \times 10^3$ W m^{-2} across the ML base (Figs. 9). The effects of turbulence were also observed in the destruction of near-surface rain layers (Fig. 13) and the continued transformation of watermass characteristics hundreds of kilometers behind the TC, where we estimated $\kappa > 10^{-3}$ m^2 s^{-1} (Fig. 15).

Insufficient spatial resolution in numerical models causes them to underestimate the intensity of TC winds (Walsh et al., 2007), subsequent upwelling, and NIW generation (Vincent et al., 2012). Likewise, it is unclear whether mixing parameterizations can reproduce the full set of impacts reported here and others that may remain undetected. For example, accurate representation of mixing in rain layers (Fig. 13) and barrier layers (Balaguru et al., 2012; Rudzin et al., 2019) is challenging but necessary to avoid biases in forecasts of storm intensity (Hlywiak & Nolan, 2019). Moreover, the long-term impacts of TC-driven NIWs on climate and ocean thermodynamics remain unresolved. Therefore, in situ and spatially resolved measurements of the ocean response to TCs are crucial to better constrain their role in global budgets of mixing and internal wave energy. This study exemplifies how data from autonomous platforms can provide a comprehensive view of the ocean response to TCs, corresponding impacts to ocean stratification, potential effects on air-sea interaction.

Acknowledgments

This work is supported by Grant NA17OAR4310259 from the Climate Variability and Predictability program at NOAA, and grants N00014163085 and N000141613073 from the Office of Naval Research's PISTON initiative, which are components of the international Years of the Maritime Continent program. We are grateful to the master, crew, and science party on *R/V Thomas Thompson* for their help in deploying floats. The Instrument Development Group at the Scripps Institution of Oceanography designed, prepared, and monitored the SOLO-II floats. N.G.B. is funded by Consejo Nacional de Ciencia y Tecnología (CONACyT) and UC Mexus. E.J.T. contributes effort with funding from the NOAA Weather Program Office's Precipitation Prediction Grand Challenge. Kristin Zeiden, Nathalie Zilberman, William R. Young, and three anonymous reviewers provided valuable comments.

Float data are available at the PISTON data site www-air.larc.nasa.gov/cgi-bin/ArcView/camp2ex?TRAJECTORY=1#JOHNSTON. SHAUN. Tropical cyclone best track data are available from the JTWC at www.usno.navy.mil/NOOC/nmfc-ph/RSS/jtwc/best_tracks/index.html. Coupled ocean-atmosphere model results are available at https://doi.org/10.5281/zenodo.4134671.

References

Alford, M. H. (2001). Internal swell generation: The spatial distribution of energy flux from the wind to mixed layer near-inertial motions. *Journal of Physical Oceanography*, *31*(8), 2359–2368.

Alford, M. H., Gregg, M. C., & Ilyas, M. (1999). Diapycnal mixing in the Banda Sea: Results of the first microstructure measurements in the Indonesian Throughflow. *Geophysical Research Letters*, *26*(17), 2741–2744.

Asselin, O., & Young, W. R. (2020, 06). Penetration of Wind-Generated Near-

Inertial Waves into a Turbulent Ocean. *Journal of Physical Oceanography*, *50*(6), 1699-1716. Retrieved from `https://doi.org/10.1175/JPO-D-19-0319.1` doi: 10.1175/JPO-D-19-0319.1

Baker, M. A., & Gibson, C. H. (1987). Sampling turbulence in the stratified ocean: Statistical consequences of strong intermittency. *Journal of Physical Oceanography*, *17*(10), 1817–1836.

Balaguru, K., Chang, P., Saravanan, R., Leung, L. R., Xu, Z., Li, M., & Hsieh, J.-S. (2012). Ocean barrier layers' effect on tropical cyclone intensification. *Proceedings of the National Academy of Sciences*, *109*(36), 14343–14347.

Cael, B., & Mashayek, A. (2021). Log-skew-normality of ocean turbulence. *Physical Review Letters*, *126*(22), 224502.

Chang, S. W., & Anthes, R. A. (1978). Numerical simulations of the ocean's nonlinear, baroclinic response to translating hurricanes. *Journal of Physical Oceanography*, *8*(3), 468–480.

Chen, S., Cummings, J. A., Schmidt, J. M., Sanabia, E. R., & Jayne, S. R. (2017). Targeted ocean sampling guidance for tropical cyclones. *Journal of Geophysical Research: Oceans*, *122*(5), 3505–3518.

Chen, S. S., & Curcic, M. (2016). Ocean surface waves in Hurricane Ike (2008) and Superstorm Sandy (2012): Coupled model predictions and observations. *Ocean Modelling*, *103*, 161–176.

D'Asaro, E. A. (1985). The energy flux from the wind to near-inertial motions in the surface mixed layer. *Journal of Physical Oceanography*, *15*(8), 1043–1059.

D'Asaro, E. A. (1989). The decay of wind-forced mixed layer inertial oscillations due to the β effect. *Journal of Geophysical Research: Oceans*, *94*(C2), 2045–2056.

D'Asaro, E. A. (2003). The ocean boundary layer below Hurricane Dennis. *Journal of Physical Oceanography*, *33*(3), 561–579.

D'Asaro, E. A., Sanford, T. B., Niiler, P. P., & Terrill, E. J. (2007). Cold wake of hurricane Frances. *Geophysical Research Letters*, *34*(15).

Davis, R., Sherman, J., & Dufour, J. (2001). Profiling ALACEs and other advances in autonomous subsurface floats. *Journal of atmospheric and oceanic technology*, *18*(6), 982–993.

Davis, R. E. (1985). Objective mapping by least squares fitting. *Journal of Geophysical Research: Oceans*, *90*(C3), 4773–4777.

Ekman, V. W. (1905). On the influence of the earth's rotation on ocean-currents.

Emanuel, K. (2001). Contribution of tropical cyclones to meridional heat transport by the oceans. *Journal of Geophysical Research: Atmospheres*, *106*(D14), 14771–14781.

Emanuel, K. (2005). Increasing destructiveness of tropical cyclones over the past 30 years. *Nature*, *436*(7051), 686–688.

Emanuel, K. A. (1999). Thermodynamic control of hurricane intensity. *Nature*, *401*(6754), 665–669.

Geisler, J. E. (1970). Linear theory of the response of a two layer ocean to a moving hurricane. *Geophysical and Astrophysical Fluid Dynamics*, *1*(1-2), 249–272.

Gill, A. (1984). On the behavior of internal waves in the wakes of storms. *Journal of Physical Oceanography*, *14*(7), 1129–1151.

Glenn, S., Miles, T., Seroka, G., Xu, Y., Forney, R., Yu, F., ... Kohut, J. (2016). Stratified coastal ocean interactions with tropical cyclones. *Nature Communications*, *7*(1), 1–10.

Guan, S., Zhao, W., Huthnance, J., Tian, J., & Wang, J. (2014). Observed upper ocean response to typhoon Megi (2010) in the Northern South China Sea. *Journal of Geophysical Research: Oceans*, *119*(5), 3134–3157.

Hautala, S. L., Reid, J. L., & Bray, N. (1996). The distribution and mixing of Pacific water masses in the Indonesian Seas. *Journal of Geophysical Research: Oceans*, *101*(C5), 12375–12389.

Hlywiak, J., & Nolan, D. S. (2019). The influence of oceanic barrier layers on tropical cyclone intensity as determined through idealized, coupled numerical simulations. *Journal of Physical Oceanography*, *49*(7), 1723–1745.

Huffman, G. J., Bolvin, D. T., Braithwaite, D., Hsu, K., Joyce, R., Xie, P., & Yoo, S.-H. (2015). NASA global precipitation measurement (GPM) integrated multi-satellite retrievals for GPM (IMERG). *Algorithm Theoretical Basis Document (ATBD) Version*, *4*, 26.

Jacob, S. D., Shay, L. K., Mariano, A. J., & Black, P. G. (2000). The 3D oceanic mixed layer response to Hurricane Gilbert. *Journal of Physical Oceanography*, *30*(6), 1407–1429.

Johnston, T. M. S., Chaudhuri, D., Mathur, M., Rudnick, D. L., Sengupta, D., Simmons, H. L., … Venkatesan, R. (2016). Decay mechanisms of near-inertial mixed layer oscillations in the Bay of Bengal. *Oceanography*, *29*(2), 180–191.

Johnston, T. M. S., & Rudnick, D. L. (2009). Observations of the transition layer. *Journal of physical oceanography*, *39*(3), 780–797.

Johnston, T. M. S., Rudnick, D. L., Brizuela, N., & Moum, J. N. (2020). Advection by the North Equatorial Current of a cold wake due to multiple typhoons in the western Pacific: Measurements from a profiling float array. *Journal of Geophysical Research: Oceans*, *125*(4), e2019JC015534.

Johnston, T. M. S., Wang, S., Lee, C.-Y., Moum, J. N., Rudnick, D. L., & Sobel, A. (2021). Near-inertial wave propagation in the wake of Super Typhoon Mangkhut: Measurements from a profiling float array. *Journal of Geophysical Research: Oceans*, e2020JC016749.

Korty, R. L., Emanuel, K. A., & Scott, J. R. (2008). Tropical cyclone–induced upper-ocean mixing and climate: Application to equable climates. *Journal of Climate*, *21*(4), 638–654.

Kundu, P. K., & Thomson, R. E. (1985). Inertial oscillations due to a moving front. *Journal of physical oceanography*, *15*(8), 1076–1084.

Kunze, E. (1985). Near-inertial wave propagation in geostrophic shear. *Journal of Physical Oceanography*, *15*(5), 544–565.

Le Traon, P., Nadal, F., & Ducet, N. (1998). An improved mapping method of multisatellite altimeter data. *Journal of atmospheric and oceanic technology*, *15*(2), 522–534.

Mater, B. D., Venayagamoorthy, S. K., St. Laurent, L., & Moum, J. N. (2015). Biases in thorpe-scale estimates of turbulence dissipation. part i: Assessments from large-scale overturns in oceanographic data. *Journal of Physical Oceanography*, *45*(10), 2497–2521.

Mei, W., Primeau, F., McWilliams, J. C., & Pasquero, C. (2013). Sea surface height evidence for long-term warming effects of tropical cyclones on the ocean. *Proceedings of the National Academy of Sciences*, *110*(38), 15207–15210.

Moum, J., Farmer, D., Smyth, W., Armi, L., & Vagle, S. (2003). Structure and generation of turbulence at interfaces strained by internal solitary waves propagating shoreward over the continental shelf. *Journal of Physical Oceanography*, *33*(10), 2093–2112.

Nagai, T., Tandon, A., Kunze, E., & Mahadevan, A. (2015). Spontaneous generation of near-inertial waves by the kuroshio front. *Journal of Physical Oceanography*, *45*(9), 2381–2406.

Névir, P., & Sommer, M. (2009). Energy–vorticity theory of ideal fluid mechanics. *Journal of the Atmospheric Sciences*, *66*(7), 2073–2084.

Nilsson, J. (1995, 04). Energy flux from traveling hurricanes to the oceanic internal wave field. *Journal of Physical Oceanography*, *25*(4), 558-573.

Osborn, T. (1980). Estimates of the local rate of vertical diffusion from dissipation measurements. *Journal of physical oceanography*, *10*(1), 83–89.

Pearson, B., & Fox-Kemper, B. (2018). Log-normal turbulence dissipation in global

ocean models. *Physical review letters*, *120*(9), 094501.
Pollard, R. T. (1970). On the generation by winds of inertial waves in the ocean. In *Deep sea research and oceanographic abstracts* (Vol. 17, pp. 795–812).
Pollard, R. T., & Millard, R. (1970). Comparison between observed and simulated wind-generated inertial oscillations. In *Deep sea research and oceanographic abstracts* (Vol. 17, pp. 813–821).
Pollard, R. T., Rhines, P. B., & Thompson, R. O. (1973). The deepening of the wind-mixed layer. *Geophysical Fluid Dynamics*, *4*(4), 381–404.
Price, J. F. (1981). Upper ocean response to a hurricane. *Journal of Physical Oceanography*, *11*(2), 153–175.
Price, J. F. (1983). Internal wave wake of a moving storm. Part I. Scales, energy budget and observations. *Journal of Physical Oceanography*, *13*(6), 949–965.
Price, J. F., Sanford, T. B., & Forristall, G. Z. (1994). Forced stage response to a moving hurricane. *Journal of Physical Oceanography*, *24*(2), 233–260.
Rudzin, J. E., Shay, L. K., & Jaimes de la Cruz, B. (2019). The impact of the Amazon–Orinoco River plume on enthalpy flux and air–sea interaction within Caribbean Sea tropical cyclones. *Monthly Weather Review*, *147*(3), 931–950.
Sanabia, E. R., & Jayne, S. R. (2020). Ocean observations under two major hurricanes: Evolution of the response across the storm wakes. *AGU Advances*, *1*(3), e2019AV000161.
Sanford, T. B., Price, J. F., & Girton, J. B. (2011). Upper-ocean response to Hurricane Frances (2004) observed by profiling EM-APEX floats. *Journal of Physical Oceanography*, *41*(6), 1041–1056.
Scotti, A. (2015). Biases in thorpe-scale estimates of turbulence dissipation. part ii: Energetics arguments and turbulence simulations. *Journal of Physical Oceanography*, *45*(10), 2522–2543.
Shay, L. K., & Chang, S. W. (1997). Free surface effects on the near-inertial ocean current response to a hurricane: A revisit. *Journal of Physical Oceanography*, *27*(1), 23–39.
Shay, L. K., Elsberry, R. L., & Black, P. G. (1989). Vertical structure of the ocean current response to a hurricane. *Journal of Physical Oceanography*, *19*(5), 649–669.
Skamarock, W. C., Klemp, J. B., Dudhia, J., Gill, D. O., Barker, D. M., Wang, W., & Powers, J. G. (2008). A description of the Advanced Research WRF version 3. NCAR Technical note-475+ STR.
Sriver, R. L., & Huber, M. (2007). Observational evidence for an ocean heat pump induced by tropical cyclones. *Nature*, *447*(7144), 577–580.
Thompson, A., Gille, S. T., MacKinnon, J. A., & Sprintall, J. (2007). Spatial and temporal patterns of small-scale mixing in Drake Passage. *Journal of Physical Oceanography*, *37*(3), 572–592.
Thompson, E. J., Moum, J. N., Fairall, C. W., & Rutledge, S. A. (2019). Wind limits on rain layers and diurnal warm layers. *Journal of Geophysical Research: Oceans*, *124*(2), 897–924.
Thorpe, S. (1977). Turbulence and mixing in a Scottish loch. *Philosophical Transactions of the Royal Society of London. Series A, Mathematical and Physical Sciences*, *286*(1334), 125–181.
Turner, J., & Kraus, E. (1967). A one-dimensional model of the seasonal thermocline i. a laboratory experiment and its interpretation. *Tellus*, *19*(1), 88–97.
Veronis, G. (1956). Partition of energy between geostrophic and non-geostrophic oceanic motions. *Deep Sea Research (1953)*, *3*(3), 157–177.
Vincent, E. M., Lengaigne, M., Madec, G., Vialard, J., Samson, G., Jourdain, N. C., ... Jullien, S. (2012). Processes setting the characteristics of sea surface cooling induced by tropical cyclones. *Journal of Geophysical Research: Oceans*, *117*(C2).
Wallcraft, A., Metzger, E., & Carroll, S. (2009). *Software design description for*

the hybrid coordinate ocean model (HYCOM), Version 2.2 (Tech. Rep.). Naval Research Lan Stennis Space Center MS Oceanography Div.

Walsh, K., Fiorino, M., Landsea, C., & McInnes, K. (2007). Objectively determined resolution-dependent threshold criteria for the detection of tropical cyclones in climate models and reanalyses. *Journal of climate*, *20*(10), 2307–2314.

Wamsley, L. (2018, Sep). Dozens more feared dead in the philippines after typhoon triggers mudslide. *National Public Radio*. Retrieved from `https://www.npr.org/2018/09/17/648866035/dozens-more-feared-dead-in-the-philippines-after-typhoon-triggers-mudslide`

Whitt, D. B., & Thomas, L. N. (2015). Resonant generation and energetics of wind-forced near-inertial motions in a geostrophic flow. *Journal of Physical Oceanography*, *45*(1), 181–208.

Zweers, N., Makin, V., De Vries, J., & Burgers, G. (2010). A sea drag relation for hurricane wind speeds. *Geophysical Research Letters*, *37*(21).